Acoustic localization of vehicular sources using distributed sensors

Mahmood R. Azimi-Sadjadi, Saravana Kumar Srinivasan, and Saeid Ahmadinia

Citation: The Journal of the Acoustical Society of America **146**, 4913 (2019); doi: 10.1121/1.5138934
View online: https://doi.org/10.1121/1.5138934
View Table of Contents: https://asa.scitation.org/toc/jas/146/6
Published by the Acoustical Society of America

Acoustic localization of vehicular sources using distributed sensors

Mahmood R. Azimi-Sadjadi,[1,a)] Saravana Kumar Srinivasan,[2] and Saeid Ahmadinia[1]
[1]*Electrical and Computer Engineering Department, Colorado State University, Fort Collins, Colorado 80523-1373, USA*
[2]*Information System Technologies Inc., Fort Collins, Colorado 80525, USA*

(Received 20 March 2019; revised 25 August 2019; accepted 22 September 2019; published online 31 December 2019)

This paper considers the problem of locating ground vehicles using their acoustic signatures recorded by unattended passive acoustic sensors. Acoustic signatures of the ground sources captured by different sensors within a cluster are used to generate direction of arrival (DoA) of the propagating wavefronts. Using the estimated DoAs of disparate distributed sensor node clusters, this paper introduced and compared several different existing target localization methods that provide the location and velocity estimates of a moving source. A robust source localization method is then proposed to account for large DoA errors and outliers which often occur in realistic settings. This method does not use any prior knowledge of the dynamical model of the moving source. The effectiveness and complexity of these methods are compared using synthesized and real acoustic signature data sets. © *2019 Acoustical Society of America*. https://doi.org/10.1121/1.5138934

[ZHM] Pages: 4913–4925

I. INTRODUCTION

Unattended passive acoustic sensors are among the widely used sensors for remote surveillance, situation awareness, and monitoring applications.[1–3] They can be used to capture acoustic signatures of a wide variety of sources including ground and airborne vehicles, as well as transient events such as gunshots. Among their benefits are simplicity and ease in deployment, large coverage area, good spatial resolution for separating multiple closely spaced sources, less hardware complexity and hence significantly lower costs, and more flexibility in configuring different dynamic sensor array configurations.

Acoustic source localization and tracking using distributed sensors have attracted considerable attention in recent years. In Ref. 4, a fast wideband algorithm for finding the bearing angle of an airborne acoustic source was proposed using a single acoustic vector sensor located on the ground. The bearing estimates from several arbitrary locations were then used in conjunction with the weighted least-squares (WLS) algorithm to determine the three-dimensional (3D) position of the source while it is in audible range of the sensor. The work in Ref. 5 presented a performance analysis of wideband source localization when bearing estimation was carried out at individual arrays and time-delay estimation was done between sensor elements on different arrays. They assumed perfect spatial coherence of the wavefront over each array and frequency-selective coherence between different arrays. Results were presented to show the accuracy of the time-delay estimation process. Sheng *et al.*[6] used an acoustic attenuation model as a function of source range to cast the source localization problem as a maximum likelihood (ML) estimation. They proposed two methods to solve this nonlinear optimization problem. The Cramer Rao Bound (CRB) analysis of localization accuracy as a function of the sensor deployment scheme was also performed. In Ref. 7, the authors considered the problem of acoustic source localization using sparsely distributed sensor networks formed by mobile wireless devices. They used time differences of arrival (TDoA) estimates for the microphone pairs while a ML estimator was used for source position estimation. The effects of the aperture of the sparse array and sensor position uncertainties on the performance of the source localization algorithm were also studied. Reference 8 reviews several common approaches to source localization in wireless sensor networks that use either source energy, time of arrival (ToA), TDoA, the direction of arrival (DoA), and/or the steered response power resulting from combining multiple microphone signals. They also discussed methods to locate the sensor nodes in a mesh network. The authors in Ref. 9 used joint measurements generated using three different methods, namely, DoA, TDoA, and gain ratio of arrival (GRoA) to quantify the performance gain compared to the existing methods. They showed that the performance gain using the combined measurements can indeed be substantial for certain geometries especially in presence of coherence loss across the arrays.

In this paper, we consider the problem of localizing moving vehicular sources using clusters of sparse randomly distributed sensors. A wideband geometrically averaged Capon method[10] is first applied to estimate DoA for each cluster of nodes. These bearing estimates are then used in conjunction with several different source localization methods that differ in their *a priori* knowledge requirements as well as their complexity. These methods use the existing least squares (LS), ML, and Total LS-based methods[11] to estimate the location of the moving sources. Additionally, we investigated the use of three different nonlinear state estimation methods, namely, the extended Kalman filters (EKF), the unscented Kalman filtering

a)Electronic mail: azimi@engr.colostate.edu

(UKF), and the particle filtering (PF)[12–15] that make use of the target dynamical model for state estimation and prediction (tracking) applications. A robust ML-based method was then proposed that uses Cauchy distribution for the measurement error distribution in order to account for the erroneous DoAs and outliers which often occur in realistic conditions due to such factors as mild to strong wind, competing background interference, coherence loss, source obstruction, etc. A consistency test was also suggested to identify and remove inconsistent DoAs for more accurate estimation prior to final localization. These methods are tested and compared on several synthesized data sets to study their performance as a function of the signal-to-noise ratio (SNR), cluster diversity, and coherence loss. The robust ML-based method proposed here is then applied to real acoustic data sets for two experiments where a light truck was localized using three clusters of randomly distributed acoustic sensor nodes.

II. SOURCE LOCALIZATION USING DISTRIBUTED SPARSE CLUSTERS OF SENSORS

In this section, we address the problem of acoustic source localization using DoAs generated from clusters of sparse randomly distributed sensor nodes. Several key issues must be pointed out.

(1) Since the estimated DoAs typically contain random measurement error, simple triangulation methods can be rendered ineffective and unreliable. Thus, statistical-based methods that estimate target location from noisy DoA measurements must be employed.
(2) The clusters must be adequately spaced to guarantee DoA diversity for accurate source localization while avoiding significant coherence loss.
(3) Since the acoustic signatures of vehicular sources (engine and tire noise) exhibit a wide range of frequencies, wideband DoA estimation methods must be employed. Here, we used the geometric averaged wideband Capon[10] algorithm mainly owing to its accuracy and reduced computational requirements. This method is briefly reviewed in the next section.
(4) Finally, this paper only considers localization of single sources in order to compare the pros and cons of all the existing algorithms and provide a simple solution that leads to accurate source localization for practical situations. Although the wideband Capon algorithms in Ref. 10 can be applied to multiple moving sources, the localization problem when the sources are closely spaced requires devising a multiple DoA association method, which is beyond the scope of this paper.

A. Geometric wideband Capon method

This algorithm computes the DoA of the moving sources using the recorded acoustic data from all the sensor nodes in a cluster in every time snapshot. Each snapshot (e.g., one second long) from the acoustic signature of the source is partitioned into K non-overlapping blocks of length N samples and a fast Fourier transform (FFT) is applied to each zero-padded block. The transformed vector of dimension M, where M is the number of sensors in a cluster, for the kth block at narrowband frequency component ω_j, $j \in [1, J]$ is denoted by $\mathbf{z}_k(\omega_j)$, $k = 1, 2, \ldots, K$. These narrowband components are used to compute the sample *spatial covariance matrix*

$$\mathrm{R}_{\mathbf{zz}}(\omega_j) = \frac{1}{K}\sum_{k=1}^{K} \mathbf{z}_k(\omega_j)\mathbf{z}_k^H(\omega_j). \tag{1}$$

The spatial covariance matrices for all the frequency bins ω_j, $j \in [1, J]$ of the source are used to generate the geometrically-averaged wideband Capon power spectrum[10]

$$\mathrm{Q}_G(\theta) = \prod_{j=1}^{J} \frac{1}{\mathbf{v}^H(\omega_j, \theta)\mathrm{R}_{\mathbf{zz}}^{-1}(\omega_j)\mathbf{v}(\omega_j, \theta)}, \tag{2}$$

where $\mathbf{v}(\omega_j, \theta)$ is the array (cluster) steering vector and θ is the azimuth angle relative to the sensor node cluster. Note that it is assumed that the source and sensors are located on the same plane, i.e., same elevation. For an arbitrary geometry sparse array with M sensors, the steering vector is $\mathbf{v}(\omega_j, \theta) = [e^{j\phi_1(\theta)}, \ldots, e^{j\phi_M(\theta)}]^T/\sqrt{M}$, where $\phi_i(\theta) = -(2\pi/\lambda_j)(x_i \sin\theta + y_i \cos\theta)$ and (x_i, y_i) are the coordinates of the ith sensor node and λ_j is the wavelength for jth frequency bin.

This aggregated power spectrum is then searched over the azimuth angle θ and the angles which maximize this function are determined to be the DoA estimates of the detected sources for that snapshot. This procedure is repeated for every time snapshot, while the source is in the audible range in order to produce successive DoA estimates which can then be used to localize and track the source.

B. Bearing-only target location estimation

In this section, three different methods for source localization from multiple estimated DoAs are introduced that differ in their prior knowledge requirements and complexity. However, their common traits are that they ignore the dynamical model of the moving source and the spatial-temporal history of the data.

The approach in Ref. 11 considers the two-dimensional (2D) target localization problem using L sensor clusters with reference elements located at positions $\mathbf{r}_l = [r_{x,l}, r_{y,l}]^T$, $l = 1, \ldots, L$. If the source is located at position $\mathbf{p} = [p_x, p_y]^T$, then the actual bearing angle of the lth cluster is given by

$$\theta_l(\mathbf{p}) = \tan^{-1}\frac{\Delta y_l}{\Delta x_l}, \quad l = 1, \ldots, L, \tag{3}$$

where $\Delta y_l = p_y - r_{y,l}$ and $\Delta x_l = p_x - r_{x,l}$. Note that the position of the source is assumed to be fixed in one snapshot. The bearing measurement (or estimated DoA) of the lth cluster is denoted by $\tilde{\theta}_l = \theta_l + \eta_l$, $l = 1, \ldots, L$ where η_l is the measurement error, which is typically modeled as a white Gaussian random variable (rv) with zero mean and variance $\sigma_{\eta_l}^2$.

1. Maximum likelihood and least squares methods

It is well-known that under the Gaussian assumption for the measurement noise, η_l, the ML estimate of the target position $\hat{\mathbf{p}}_{ML}$ coincides with its LS estimate, i.e.,

$$\hat{\mathbf{p}}_{ML} = \hat{\mathbf{p}}_{LS} = \arg\min_{\mathbf{p}} J_{ML}(\mathbf{p}), \tag{4}$$

where the cost function $J_{ML}(\mathbf{p})$[11] is

$$J_{ML}(\mathbf{p}) = \sum_{l=1}^{L} \frac{1}{2\sigma_{\eta_l}^2} (\tilde{\theta}_l - \theta_l(\mathbf{p}))^2. \tag{5}$$

However, in this case, the cost function is nonlinear in $\mathbf{p}$ and hence the problem must be solved iteratively by using the gradient-descent method or other nonlinear solution finding methods.[17]

Alternatively, this nonlinear problem can be transformed into a linear one by assuming that the measurement errors, $\tilde{\theta}_l - \theta_l, \forall l$ are very small, in which case we can approximate them by $\tilde{\theta}_l - \theta_l \approx \sin(\tilde{\theta}_l - \theta_l)$. Clearly, in situations where this assumption is not valid, this estimator becomes unreliable. Substituting this approximation into Eq. (5) gives the cost function[11]

$$\begin{aligned} J_{LS}(\mathbf{p}) &= \sum_{l=1}^{L} \frac{1}{2\sigma_{\eta_l}^2} \sin^2(\tilde{\theta}_l - \theta_l(\mathbf{p})) \\ &= \frac{1}{2}(\mathbf{A}\mathbf{p} - \mathbf{b})^T \mathbf{W}^{-1} (\mathbf{A}\mathbf{p} - \mathbf{b}), \end{aligned} \tag{6}$$

where $\mathbf{A}$ is the $L \times 2$ matrix given by $\mathbf{A} = [\mathbf{a}_1, \mathbf{a}_2, \ldots, \mathbf{a}_L]^T$, with $\mathbf{a}_l = [\sin\tilde{\theta}_l, -\cos\tilde{\theta}_l]^T$, $\mathbf{b}$ is the $L \times 1$ vector $\mathbf{b} = [\mathbf{a}_1^T\mathbf{r}_1, \mathbf{a}_2^T\mathbf{r}_2, \ldots, \mathbf{a}_L^T\mathbf{r}_L]^T$, and $\mathbf{W}$ is the $L \times L$ diagonal weighting matrix, $\mathbf{W} = diag[d_1^2\sigma_{\eta_1}^2, d_2^2\sigma_{\eta_2}^2, \ldots, d_L^2\sigma_{\eta_L}^2]$, where d_l is the distance between the target position $\mathbf{p}$ and the reference node of lth cluster $\mathbf{r}_l$, i.e., $d_l = \sqrt{(\Delta x_l)^2 + (\Delta y_l)^2}$.

Then, the solution to this problem becomes

$$\hat{\mathbf{p}}_{LS} = \arg\min_{\mathbf{p}} J_{LS}(\mathbf{p}) = (\mathbf{A}^T\mathbf{W}^{-1}\mathbf{A})^{-1}\mathbf{A}^T\mathbf{W}^{-1}\mathbf{b}. \tag{7}$$

The weighting matrix $\mathbf{W}$ weights different measurements depending on the distance of clusters from source and noise variance. However, the target location $\mathbf{p}$ is unknown and further $\sigma_{\eta_l}^2$'s may not be available either. Thus, $\mathbf{W}$ is simply replaced by an identity matrix leading to

$$\hat{\mathbf{p}}_{LS} = (\mathbf{A}^T\mathbf{A})^{-1}\mathbf{A}^T\mathbf{b}, \tag{8}$$

which is the standard LS solution assuming unknown but deterministic measurement noise. Thus, unlike the ML-based method it does not require the knowledge of variance of measurement noise, $\sigma_{\eta_l}^2$'s.

As discussed in Ref. 11, the ML (or LS)-based methods are biased estimators, and thus usually not useful for target localization applications, especially when the variance of bearing noise is large. Moreover, outliers and false DoAs can have detrimental effects on the accuracy of the estimates. Nonetheless, the LS-based solution could still be useful for choosing the initial point for the numerical optimization algorithm employed by other methods. Note that the LS-based bearing-only target localization is the simplest method that requires the least amount of prior information to estimate the target location from the measured DoAs. In Sec. II C, we introduce other estimators that can potentially offer better localization accuracy but they require more prior knowledge to build the estimators.

2. Total least squares method

The LS approach relies heavily on the accuracy of the measurement model. In the absence of an accurate model, the goodness of estimates is sacrificed. The use of total least squares (TLS) method for bearing-only target localization was proposed in Ref. 11, where it was shown that the TLS method is robust to errors in both the measurements and sensor locations. The TLS method is based on the singular value decomposition (SVD) of the augmented $L\times$ 3 matrix $[\mathbf{A} - \mathbf{b}]$, where $\mathbf{A}$ and $\mathbf{b}$ were defined before. Taking the SVD of $[\mathbf{A} - \mathbf{b}]$ yields

$$[\mathbf{A} - \mathbf{b}] = \mathbf{U}\Sigma\mathbf{V}^{\mathbf{H}}, \tag{9}$$

where $\mathbf{U} = [\mathbf{u}_1\mathbf{u}_2\mathbf{u}_3]$ is a $L\times$ 3 unitary matrix, $\mathbf{V} = [\mathbf{v}_1\mathbf{v}_2\mathbf{v}_3]$ is a 3×3 unitary matrix, and $\mathbf{\Sigma} = diag(\sigma_1, \sigma_2, \sigma_3)$, i.e., a 3×3 diagonal matrix of singular values σ_is of $[\mathbf{A} - \mathbf{b}]$. Using the rank-2 approximation of the perturbed augmented matrix $[\mathbf{A} - \mathbf{b}]$ in Ref. 11, they showed that estimate of target location using the TLS leads to

$$\hat{\mathbf{p}}_{TLS} = \frac{1}{v_{33}}[v_{13}v_{23}]^T, \tag{10}$$

where $\mathbf{v}_3 = [v_{13}, v_{23}, v_{33}]^T$ is the third column of unitary matrix $\mathbf{V}$.

C. Bearing-only target location and velocity estimation

The source localization algorithms discussed thus far only use a single or a small set of observations to produce the location estimates and hence ignore the temporal history of the moving source. In contrast, the methods described in this section not only make use of the prior observations but also the dynamical model of the moving source to generate estimates of its position and velocity at every time instance. This could be a benefit in situations where the model and observations are reliable and a major negative when they are not. These issues will be illustrated in the simulation result Sec. III A.

Here, owing to the nonlinear nature of the problem, we employed three different nonlinear state estimation methods, namely, the extended Kalman filter (EKF), the unscented Kalman filter (UKF), and the particle filter (PF). These methods, which have successfully been applied[13–15] to similar problems before, are briefly reviewed next.

1. EKF

To apply the EKF to our application, we define the bearing-only location and velocity estimation problem as state estimation or prediction (for tracking) with state and observation equations[13,14]

$$\begin{cases} \mathbf{x}(k+1) = \mathbf{F}\mathbf{x}(k) + \mathbf{G}\mathbf{w}(k) \\ \mathbf{y}(k) = \mathbf{h}(\mathbf{x}(k)) + \mathbf{n}(k). \end{cases} \tag{11}$$

Here, $\mathbf{x}(k) = [p_{x,k}, p_{y,k}, v_{x,k}, v_{y,k}]^T$ represents the state vector at time k (discrete-time) containing the position and velocity components of the source, $\mathbf{w}(k)$ represents the driving process, $\mathbf{n}(k)$ represents the additive measurement noise vector, and $\mathbf{y}(k) = [\tilde{\theta}_1(k), \ldots, \tilde{\theta}_L(k)]^T$ is the observation vector containing the estimated DoAs of the L clusters at time k. The driving process $\mathbf{w}(k)$ and the additive noise $\mathbf{n}(k)$ are assumed to be zero mean with known covariance matrices $\mathbf{Q}_w$ and $\mathbf{Q}_n$, respectively.

Using T to denote the time difference between successive times when bearing measurements are received, matrices $\mathbf{F}$ and $\mathbf{G}$ that capture the target dynamical model are given by

$$\mathbf{F} = \begin{bmatrix} 1 & 0 & T & 0 \\ 0 & 1 & 0 & T \\ 0 & 0 & 1 & 0 \\ 0 & 0 & 0 & 1 \end{bmatrix} \quad \text{and} \quad \mathbf{G} = \begin{bmatrix} 0.5T^2 & 0 \\ 0 & 0.5T^2 \\ T & 0 \\ 0 & T \end{bmatrix}.$$

While the state equation is linear, the observation $\mathbf{y}(k)$ is a nonlinear function of the state vector $\mathbf{x}(k)$. That is, the nonlinear function $\mathbf{h}(\mathbf{x}(k))$ in Eq. (11) is the inverse tangent function that maps the state vector to the DoA measurement vector, i.e.,

$$\tilde{\theta}_l(k) = \tan^{-1}\left(\frac{p_{y,k} + Tv_{y,k} - r_{y,l}}{p_{x,k} + Tv_{x,k} - r_{x,l}}\right) + n_l(k), \quad l = 1, \ldots, L. \tag{12}$$

The EKF uses the Taylor series expansion, truncated at the first order, to linearize the non-linear observation equation in Eq. (11). Using $\hat{\mathbf{x}}(k|k)$ to denote the estimate of the state vector at time k, given all the observations up to and including $\mathbf{y}(k)$ and $\mathbf{P}(k|k)$ to represent the *a posteriori* (after updating) error covariance matrix of $\hat{\mathbf{x}}(k|k)$, the EKF equations[13,14] in order of implementation are given below:

$$\hat{\mathbf{x}}(k|k-1) = \mathbf{F}\hat{\mathbf{x}}(k-1|k-1) \quad \text{initial estimate (prediction) step,} \tag{13}$$

$$\mathbf{P}(k|k-1) = \mathbf{F}\mathbf{P}(k-1|k-1)\mathbf{F}^T + \mathbf{G}\mathbf{Q}_w\mathbf{G}^T \quad \textit{a priori} \text{ error covariance matrix,} \tag{14}$$

$$\mathbf{K}(k) = \mathbf{P}(k|k-1)\mathbf{M}^T(k)[\mathbf{M}(k)\mathbf{P}(k|k-1) \times \mathbf{M}^T(k) + \mathbf{Q}_n]^{-1} \quad \text{Kalman Gain matrix,} \tag{15}$$

where $\mathbf{M}(k) = \nabla\mathbf{h}(\hat{\mathbf{x}}(k|k-1))$ is the $L \times 4$ Jacobian matrix of the $\tan^{-1}$ functions, evaluated at the initial state estimate $\hat{\mathbf{x}}(k|k-1)$,

$$\hat{\mathbf{x}}(k|k) = \hat{\mathbf{x}}(k|k-1) + \mathbf{K}(k)[\mathbf{y}(k) - \hat{\mathbf{y}}(k|k-1)] \quad \text{State update,} \tag{16}$$

where $\hat{\mathbf{y}}(k|k-1) = \mathbf{h}(\hat{\mathbf{x}}(k|k-1))$ is the predicted observation vector,

$$\mathbf{P}(k|k) = [\mathbf{I} - \mathbf{K}(k)\mathbf{M}(k)]\mathbf{P}(k|k-1) \quad \textit{a posteriori} \text{ error covariance matrix.} \tag{17}$$

As mentioned in Refs. 12–14, the EKF reaches within the first-order approximation of the state vector since the nonlinear function is approximated using only the Jacobian. The inaccuracy problems in the EKF can be overcome by using the UKF and PF reviewed next.

2. UKF

Unlike the EKF, which uses the Jacobian to approximate the nonlinear observation function, the UKF attempts to capture the distribution of the state vector. This is done using a set of deterministically chosen *sigma points* to capture the mean and covariance of the distribution. The UKF algorithm is based on the unscented transformation,[12] which chooses $2N+1$ points, using the N-dimensional state estimate vector, $\hat{\mathbf{x}}(k-1|k-1)$, and its error covariance $\mathbf{P}(k-1|k-1)$. The $2N+1$ chosen initial sigma points $\chi_i(k-1|k-1)$ and their corresponding weights W_i are given by

$$\begin{aligned} &\chi_0(k-1|k-1) = \hat{\mathbf{x}}(k-1|k-1), \quad W_0 = \frac{\kappa}{N+\kappa}, \\ &\chi_i(k-1|k-1) = \hat{\mathbf{x}}(k-1|k-1) + \gamma\left[\sqrt{\mathbf{P}(k-1|k-1)}\right]_i, \\ &W_i = \frac{1}{2(N+\kappa)}, \quad \text{for } i = 1, \ldots, N, \\ &\chi_i(k-1|k-1) = \hat{\mathbf{x}}(k-1|k-1) - \gamma\left[\sqrt{\mathbf{P}(k-1|k-1)}\right]_i, \\ &W_i = \frac{1}{2(N+\kappa)}, \quad \text{for } i = N+1, \ldots, 2N, \end{aligned} \tag{18}$$

where $[\sqrt{\mathbf{P}(k-1|k-1)}]_i$ is the ith column of the square root matrix (e.g., Cholesky factor[18]) of $\mathbf{P}(k-1|k-1)$, and $\gamma = \sqrt{(N+\kappa)}$ with κ (here $\kappa = 1$ is used) being a scaling factor that determines the spread of sigma points around $\hat{\mathbf{x}}(k-1|k-1)$.

The initial sigma points are transformed through the state equation to yield

$$\chi_i^*(k|k-1) = \mathbf{F}\chi_i(k-1|k-1), \quad i = 0, \ldots, 2N. \tag{19}$$

Weighted sums of these transformed sigma points are used to generate the initial state vector estimate $\hat{\mathbf{x}}(k|k-1)$ and the *a priori* error covariance matrix $\mathbf{P}(k|k-1)$

$$\begin{aligned} \hat{\mathbf{x}}(k|k-1) &= \sum_{i=0}^{2N} W_i\chi_i^*(k|k-1), \\ \mathbf{P}(k|k-1) &= \sum_{i=0}^{2N} W_i\left[\chi_i^*(k|k-1) - \hat{\mathbf{x}}(k|k-1)\right] \\ &\quad \times \left[\chi_i^*(k|k-1) - \hat{\mathbf{x}}(k|k-1)\right]^T + \mathbf{G}\mathbf{Q}_w\mathbf{G}^T. \end{aligned} \tag{20}$$

New sigma points $\chi_i(k|k-1)$ are generated using $\hat{\mathbf{x}}(k|k-1)$ and $\mathbf{P}(k|k-1)$ as in Eq. (18). These new sigma points are

then propagated through the nonlinear $\tan^{-1}$ function Eq. (12) to obtain

$$\mathcal{Z}_i(k|k-1) = \mathbf{h}(\chi_i(k|k-1)),\ i = 0, \ldots, 2N. \tag{21}$$

The predicted measurement vector $\hat{\mathbf{y}}(k|k-1)$ is computed using

$$\hat{\mathbf{y}}(k|k-1) = \sum_{i=0}^{2N} W_i \mathcal{Z}_i(k|k-1). \tag{22}$$

The Kalman gain is then computed using

$$\mathbf{K}(k) = \mathbf{P}_{xz}\mathbf{P}_{zz}^{-1}, \tag{23}$$

where

$$\mathbf{P}_{xz} = \sum_{i=0}^{2N} W_i[\chi_i(k|k-1) - \hat{\mathbf{x}}(k|k-1)] \times [\mathcal{Z}_i(k|k-1) - \hat{\mathbf{y}}(k|k-1)]^T, \tag{24}$$

$$\mathbf{P}_{zz} = \sum_{i=0}^{2N} W_i[\mathcal{Z}_i(k|k-1) - \hat{\mathbf{y}}(k|k-1)] \times [\mathcal{Z}_i(k|k-1) - \hat{\mathbf{y}}(k|k-1)]^T + \mathbf{Q}_n. \tag{25}$$

The update equations for the UKF are then

$$\hat{\mathbf{x}}(k|k) = \hat{\mathbf{x}}(k|k-1) + \mathbf{K}(k)[\mathbf{y}(k) - \hat{\mathbf{y}}(k|k-1)], \tag{26}$$

$$\mathbf{P}(k|k) = \mathbf{P}(k|k-1) - \mathbf{K}(k)\mathbf{P}_{zz}\mathbf{K}^T(k). \tag{27}$$

Both EKF and UKF start by initializing the state vector estimate $\hat{\mathbf{x}}(0|0)$ as the mean vector of data and the corresponding error covariance matrix $\mathbf{P}(0|0)$ as an identity matrix.

3. PF

In may ways, PF is similar to the UKF and can be viewed as a non-parametric Bayes filter.[15,16] However, unlike UKF, which uses sigma points, PF exploits the concept of *sequential important sampling* of the unknown state to approximate posterior probability densities. More specifically, PF approximates the posterior distributions by using samples which are called particles $\mathbf{x}^1(k), \mathbf{x}^2(k), \ldots, \mathbf{x}^M(k)$, where M and k are the number of particles and time step, respectively. The goal of particle filtering is to approximate the posterior distribution at time k, i.e., the *target distribution*, from the posterior distribution at time $k-1$ through using the so-called *proposal or importance distribution*. The proposal distribution is basically the distribution of particles fed into the state equation. PF implementation includes the following four stages:

(1) Draw particles from the proposal distribution $\mathbf{x}^m(k) \sim p(\mathbf{x}(k)|\mathbf{x}^{1:M}(k-1))$ represented by particles $\mathbf{x}^1(k-1), \mathbf{x}^2(k-1), \ldots, \mathbf{x}^M(k-1)$ at time $k-1$. The updated particles are calculated by substituting the particles at time $k-1$ into the state Eq. (11),

$$\mathbf{x}^m(k|k-1) = \mathbf{F}\mathbf{x}^m(k-1). \tag{28}$$

The particles are drawn from the proposal distribution and they just need to be weighed in order to approximate the target distribution [see step (3)]. Note that particles at the first time step are drawn from a uniform distribution around the possible range of the state vector with equal weights.

(2) Predict the next measurement using the observation Eq. (12) for each particle

$$\hat{\mathbf{y}}^m(k|k-1) = \mathbf{h}(\mathbf{x}^m(k|k-1)). \tag{29}$$

(3) Compare the predicted measurement, $\hat{\mathbf{y}}^m(k|k-1)$, for each particle to the actual measurement $\mathbf{y}(k)$ at time k to weight the particles. The weight for each particle is equal to the ratio of the target distribution to the proposal distribution ratio. It can be shown that the weight update is[16]

$$w_k^m = \frac{\textit{Target Distribution}}{\textit{Proposal Distribution}} = p(\mathbf{y}(k)|\hat{\mathbf{y}}^m(k|k-1)). \tag{30}$$

The weights are normalized so that $\sum_{m=1}^{M} w_k^m = 1$. For simplicity, the distribution $p(\mathbf{y}(k)|\hat{\mathbf{y}}^m(k|k-1))$ is considered to be normal with the mean vector $\mathbf{y}(k)$ and identity covariance matrix. The updated state vector at time k is then

$$\hat{\mathbf{x}}(k|k) = \sum_{m=1}^{M} w_k^m \mathbf{x}^m(k|k-1). \tag{31}$$

(4) Resample the particles with respect to their weights to approximate the target distribution. The particles with higher weight are more frequently chosen and the particles with low weight are neglected,

$$\mathbf{x}^{1:M}(k) = \textit{Resampling}\,\{(\mathbf{x}^1(k|k-1), w_k^1), \ldots, (\mathbf{x}^M(k|k-1), w_k^M)\}. \tag{32}$$

4. A robust ML-based method

In this section, we propose a new robust ML-based source localization algorithm for scenarios where some of the bearing measurements contain large errors, *outliers*, or are simply unreliable. Such cases cannot successfully be handled by other estimators. Also, our goal is to estimate the target location $\mathbf{p} = [p_x, p_y]^T$ and velocity $\mathbf{v} = [v_x, v_y]^T$ at every snapshot. This is done by using the bearing measurements $\tilde{\theta}_l$, $l = 1, \ldots, L$ at the current time t as well as the previous times within an observation period.

The bearing angle at the lth sub-array for time instant t is given by

$$\theta_l(t) = \tan^{-1}\frac{p_{y,0} + tv_y - r_{y,l}}{p_{x,0} + tv_x - r_{x,l}}, \quad l = 1, \ldots, L,\ t = 1, \ldots, T, \tag{33}$$

where T is the total observations used to determine the current location of the source and $\mathbf{p}_0 = [p_{x,0}, p_{y,0}]^T$ is the initial location of the source at the time instant prior to the T seconds. Note that in this formulation, the velocity $\mathbf{v}$ is assumed to be constant over the entire T second time interval. Thus, if

a source is accelerating or decelerating care must be taken in choosing a time interval T that is small enough so that the source velocity is nearly constant over that interval.

As in Sec. II B 1, the bearing measurement at the lth sensor cluster at time t is denoted by $\tilde{\theta}_l(t) = \theta_l(t) + \eta_l(t)$, $l = 1, \ldots, L$, where $\eta_l(t)$ is the measurement error, which is typically considered as independent Gaussian rv with zero mean and variance $\sigma^2_{\eta_l}$. However, in practice, the distribution of the measurement error may be different from Gaussian. For example, it is typical in practical scenarios that some sensors have quite accurate bearing estimates, while the others yield erroneous or unreliable estimates due to the environment in which they operate. In Eq. (5), even the failure of one sensor can lead to inaccurate estimates. That is, the method is sensitive to the presence of large errors and outliers which will have detrimental effects on the accuracy of localization.

Thus, to make the location estimate robust against unreliable DoA estimates, we model the measurement errors η_l as rv with Cauchy distribution, $f(\eta_l) = 1/\pi(1+\eta_l^2)$. Figure 1(a) shows a Gaussian distribution with mean zero and unity variance together with a Cauchy distribution. As can be seen, compared to the Gaussian, Cauchy distribution has much heavier "tails." This heavy tail allows for better ability to account for the effects of erroneous measurements or outliers.

Based on the Cauchy distribution assumption for the bearing estimation errors, we derive the ML estimator of the source state $\mathbf{q} = [p_{x,0}, p_{y,0}, v_x, v_y]^T$,

$$\hat{\mathbf{q}}_{ML} = \arg\max_{\mathbf{q}} \prod_{t=1}^{T} \prod_{l=1}^{L} f(\eta_l(t)). \tag{34}$$

Alternatively, using the log operation, Eq. (34) can be simplified to

$$\hat{\mathbf{q}}_{ML} = \arg\min_{\mathbf{q}} \sum_{t=1}^{T} \sum_{l=1}^{L} \frac{1}{2\sigma^2_{n_{l(t)}}} \log\left[1 + (\tilde{\theta}_l(t) - \theta_l(\mathbf{q}, t))^2\right]. \tag{35}$$

It is evident that even if the lth cluster has an erroneous DoA estimate [i.e., a very large $\eta_l(t)$], the detrimental influence is deemphasized by the function $\log(1+\eta_l^2(t))$. Hence, the overall cost function will not blow up. This is illustrated in Fig. 1(b), which shows that the increase in $\log(1+\eta_l^2(t))$ is much more mild than $\eta_l(t)^2$ as $\eta_l(t)$ increases. This clearly explains why the proposed ML-based estimation based on Cauchy distribution assumption is more robust against the outliers. It is interesting to note that for very small $\eta_l(t)$, the term $\log(1+\eta_l^2(t)) \approx \eta_l^2(t)$. That is, the cost function of the robust source localization method reduces to that of the standard ML using Gaussian distribution when all the DoA estimates are reasonably good. As before, minimization of Eq. (35) can be achieved using the gradient-descent procedure or other nonlinear solvers.[17]

To further improve the accuracy of source localization method in this section, a consistency test can be devised to prevent any unreliable measurement to enter the estimation process. The steps of the consistency test go like this.

Let $\mathbf{S} = \{\tilde{\theta}_l(t)\}$ be the set of DoA estimates over the observation period $t = 1, \ldots, T$ from clusters $l = 1, \ldots, L$.

(1) Apply the robust source localization algorithm using Eq. (35) to the selected DoA estimates in set $\mathbf{S}$ to yield the vector $\hat{\mathbf{q}}_{ML}$.
(2) Based upon the estimated source position, recompute the DoAs $\{\hat{\theta}_l(t)\}$ as observed by the clusters using Eq. (33).
(3) Compute the *consistency measure*

$$C(\hat{\mathbf{q}}_{ML}, \mathbf{S}) = \frac{1}{|\mathbf{S}|} \mathbf{count}_{l,t}\Big(|\hat{\theta}_l(t) - \tilde{\theta}_l(t)| \le \delta\Big), \tag{36}$$

where δ is an upper bound on the DoA uncertainty and $|\mathbf{S}|$ represents the cardinality of set $\mathbf{S}$. This consistency function computes the number of DoA measurements that agree with the estimated source location with an uncertainty δ.

(4) If $C(\hat{\mathbf{q}}_{ML}, \mathbf{S}) = 1$, then all the DoA measurements agree with the estimated location and hence $\hat{\mathbf{q}}_{ML}$ is taken as the final estimate vector. If $C(\hat{\mathbf{q}}_{ML}, \mathbf{S}) \neq 1$, then proceed to the next step.
(5) Define the set $\mathbf{S}_{lt} = \mathbf{S} \backslash \tilde{\theta}_l(t)$, $\forall\, l$ and t which is the subset of DoA measurements with the measurement $\tilde{\theta}_l(t)$ being removed.
(6) Re-estimate the source location using the DoA measurements in the set $\mathbf{S}_{lt}$ and compute the consistency function $C(\hat{\mathbf{q}}_{ML}, \mathbf{S}_{lt})$.
(7) Find $C_{\max} = \max_{l,t} C(\hat{\mathbf{q}}_{ML}, \mathbf{S}_{lt})$ and $\mathbf{S}_{best} = \arg\max_{\mathbf{S}_{lt}} C(\hat{\mathbf{q}}_{ML}, \mathbf{S}_{lt})$.

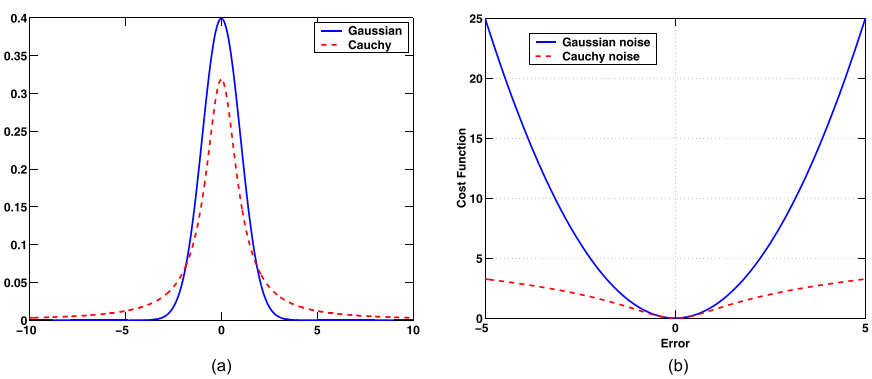

FIG. 1. (Color online) (a) The Gaussian and Cauchy distributions. (b) The DoA measurement errors $\eta_l(t)^2$ and $\log(1+\eta_l(t)^2)$ corresponding to the Gaussian and Cauchy distributions. As $\eta_l(t)$ increases, the increase in $\log(1+\eta_l(t)^2)$ is much milder than that of $\eta_l(t)^2$.

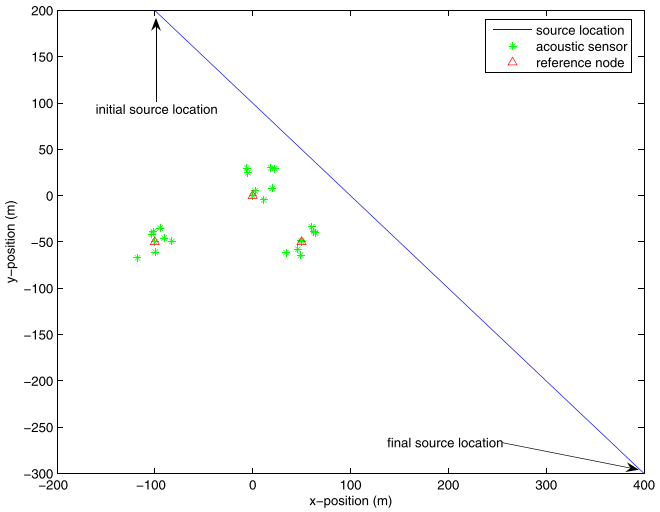

FIG. 2. (Color online) Layout of the sensor clusters and path of the moving target.

(8) If $C_{max} = 1$, then the estimated source location corresponding to $\mathbf{S}_{best}$ is taken as the final location estimate. If $C_{\max} \neq 1$, then reset $\mathbf{S} = \mathbf{S}_{best}$ and proceed to step (5).

III. SOURCE LOCALIZATION RESULTS

A. Simulation results and comparison of different methods

In order to test the source localization algorithms introduced in this paper, a simulated case of a moving ground vehicle was generated for a scenario where there are three ($L = 3$) sparse randomly distributed sensor clusters recording the acoustic data. The reference nodes of the clusters are located (in meters) at $\mathbf{r}_1 = [0, 0]^T$, $\mathbf{r}_2 = [50, -50]^T$, and $\mathbf{r}_3 = [-100, -50]^T$. Each cluster contained eight acoustic sensor nodes, randomly distributed in a 20×20 m area around the respective reference node. A single narrow-band acoustic source with a frequency of 128 Hz was simulated. The source starts at initial location $\mathbf{p}_i = [-100, 200]^T$ (in meters) and moves at a constant velocity of $\mathbf{v} = [5, -5]^T$ (m/s) over a 100 s period. Figure 2 shows the positions of the nodes in each cluster with respect to the path of the vehicle. To implement acoustic transmission loss (TL) which occurs in realistic conditions, the method in Ref. 19 was used to simulate TL for each sensor's signal based on the distance of the source to the sensor as well as several environmental parameters. It is also assumed that the location of each sensor node is known only to within an accuracy circle with radius 0.33 m that is typical for inexpensive commercial GPS systems. These sources of error, together with additive noise with varying SNR (due to acoustic TL), result in erroneous and inconsistent DoA estimates.

The bearing measurements were generated at every one second snapshot for each cluster by using the narrowband Capon beamforming. The estimated DoAs are used in conjunction with the methods covered in this paper to generate source location estimates at every one second snapshot. These location estimates are then used to plot the estimated source range, i.e., $d = \sqrt{p_x^2 + p_y^2}$, during the entire observation period of 100 s for different SNR cases at the closet point of approach (CPA).

To evaluate these localization algorithms more quantitatively, the root mean square error (RMSE) measure was also computed over the observation period. Let $\mathbf{p}$ be the true source position and $\hat{\mathbf{p}}$ be the estimated position. Now, defining the error bias as $\boldsymbol{\beta} = E[\mathbf{e}] = E[\mathbf{p} - \hat{\mathbf{p}}]$ and the error covariance matrix $\mathbf{C} = E[(\mathbf{e} - \boldsymbol{\beta})(\mathbf{e} - \boldsymbol{\beta})^T]$, then the RMSE of

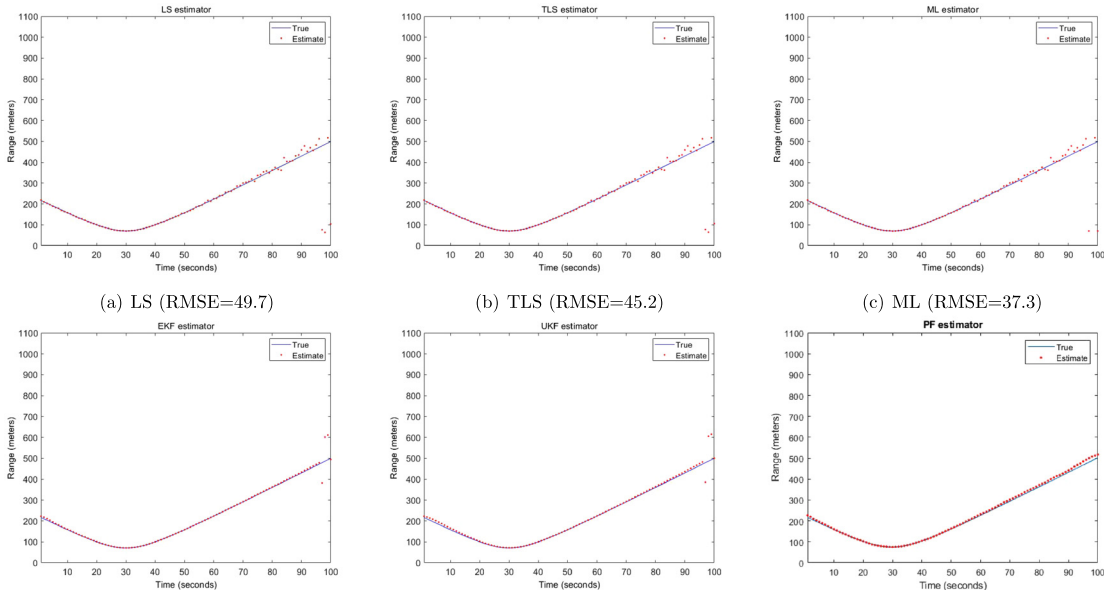

(a) LS (RMSE=49.7) (b) TLS (RMSE=45.2) (c) ML (RMSE=37.3)

(d) EKF (RMSE=13.3) (e) UKF (RMSE=12.1) (f) PF (RMSE=6.4)

FIG. 3. (Color online) Range estimation results of the different localization methods, SNR = 5 dB. (a) LS (RMSE = 49.7), (b) TLS (RMSE = 45.2), (c) ML (RMSE = 37.3), (d) EKF (RMSE = 13.3), (e) UKF (RMSE = 12.1), and (f) PF (RMSE = 6.4).

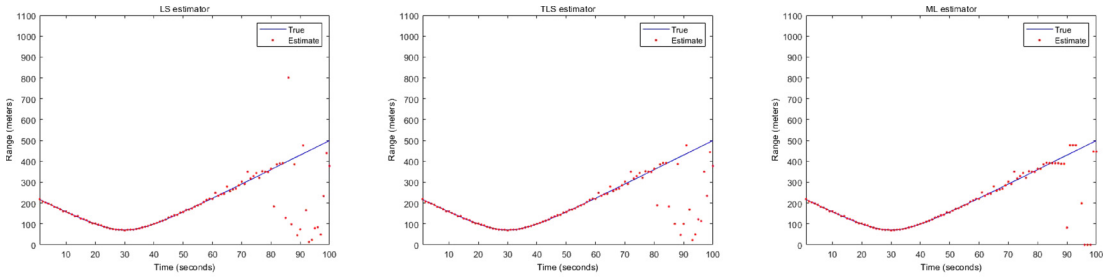

(a) LS (RMSE=197.6) (b) TLS (RMSE=356.7) (c) ML (RMSE=102.1)

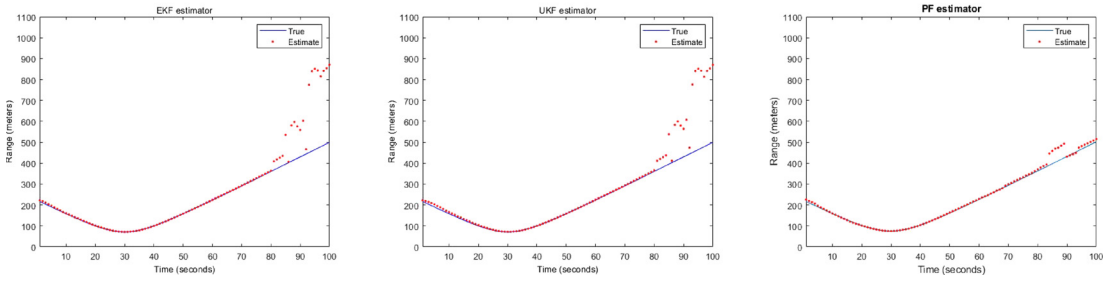

(d) EKF (RMSE=97.6) (e) UKF (RMSE=93.3) (f) PF (RMSE=33.4)

FIG. 4. (Color online) Range estimation results of the different localization methods, SNR = 0 dB. (a) LS (RMSE = 197.6), (b) TLS (RMSE = 356.7), (c) ML (RMSE = 102.1), (d) EKF (RMSE = 97.6), (e) UKF (RMSE = 93.3), and (f) PF (RMSE = 33.4).

the source position is given by[20] $\rho_{RMSE} = \sqrt{||\boldsymbol{\beta}||^2 + tr(\mathbf{C})}$, where $tr(\mathbf{C})$ is the trace of matrix $\mathbf{C}$.

Figures 3(a)–3(f) display the plots of the true (solid blue) and estimated (dotted red) source range together with the associated RMSE for the six methods and for the case where SNR = 5 dB at the CPA to the sensor nodes. Clearly, the SNR is lower at locations farther from the source due to TL effects. As can be seen from Figs. 3(a)–3(c), among the first three methods, i.e., LS, TLS, and the robust ML algorithms, the latter provided the best overall results. Additionally, at close ranges, all methods appear to have similar performance, whereas at far ranges (>200 m) when the propagation loss is more severe, the EKF, UKF, and PF algorithms clearly outperformed the LS, TLS, and ML-localization algorithms with PF providing the lowest RMSE. This improvement can be attributed to the fact that the last three methods rely on the knowledge of the source dynamical model. Moreover, EKF, UKF, and PF methods utilize all the current and previous observations as opposed to the first three methods that only use one or a limited set of observations. Consequently, the former methods are able to down-weight DoAs that are inconsistent with the trend. It must be pointed out that in practical scenarios, the source model parameters are not known and hence have to be estimated every time prior to state estimation. Otherwise, the uncertainties in the model can substantially degrade the quality of source localization for these methods. This will be shown later in this section.

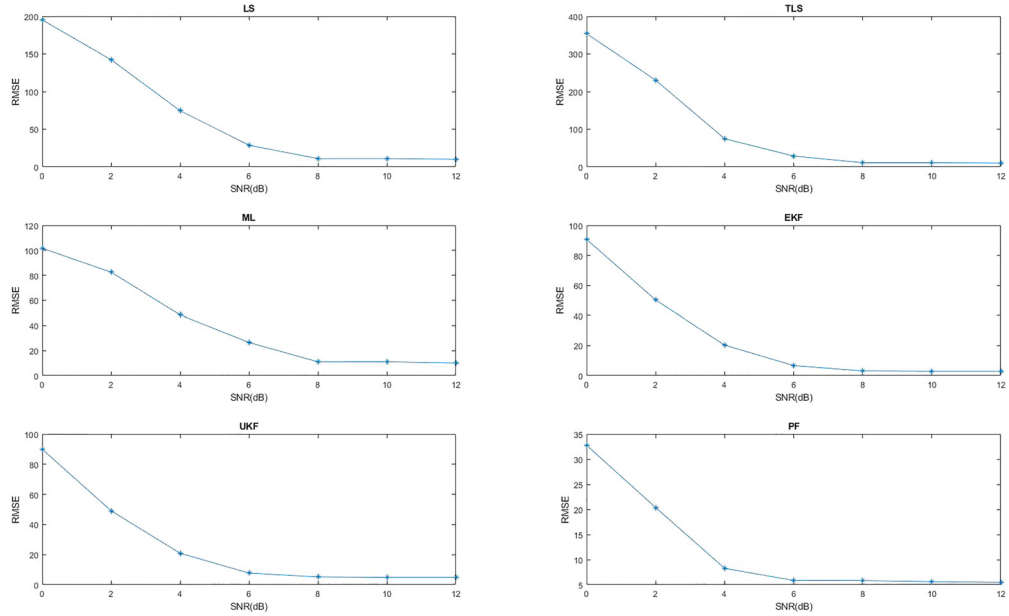

FIG. 5. (Color online) RMSE of source localization versus SNR for each algorithm.

Figures 4(a)–4(f) show plots of the range estimates of the various localization algorithms and their associated RMSE for the case where SNR = 0 dB at the CPA to the sensor nodes. As can be noticed, lower SNR together with uncertainties in the sensor location results in erroneous DoA estimates, which in turn affect the accuracy of the range estimates. The accuracy of the LS, TLS, and ML estimates start deteriorating around 60 s and that of EKF, UKF, and PF around 85 s. Again, the PF method provided the lowest overall RMSE and best results even at far ranges. This is due to the fact that PF used $M = 2500$ particles, hence capable to accurately represent the posterior distributions using the corresponding model data in both cases.

To further investigate the effect of SNR on the localization performance, the RMSE values of the location estimates are plotted as a function of SNR for each algorithm. Figure 5 shows the averaged, over 20 trials, RMSE for each algorithm, where in each trial different random realizations of sensor positions and additive noise were selected. Several interesting observations can be made. First, as can be seen, when SNR decreases beyond 6 dB, the rate of performance degradation varies significantly for different algorithms with the best one being the PF and the worst one being the TLS. Second, for all the algorithms considered here, increasing the SNR above 8 dB has very little impact on improving the performance. This is due to the fact that

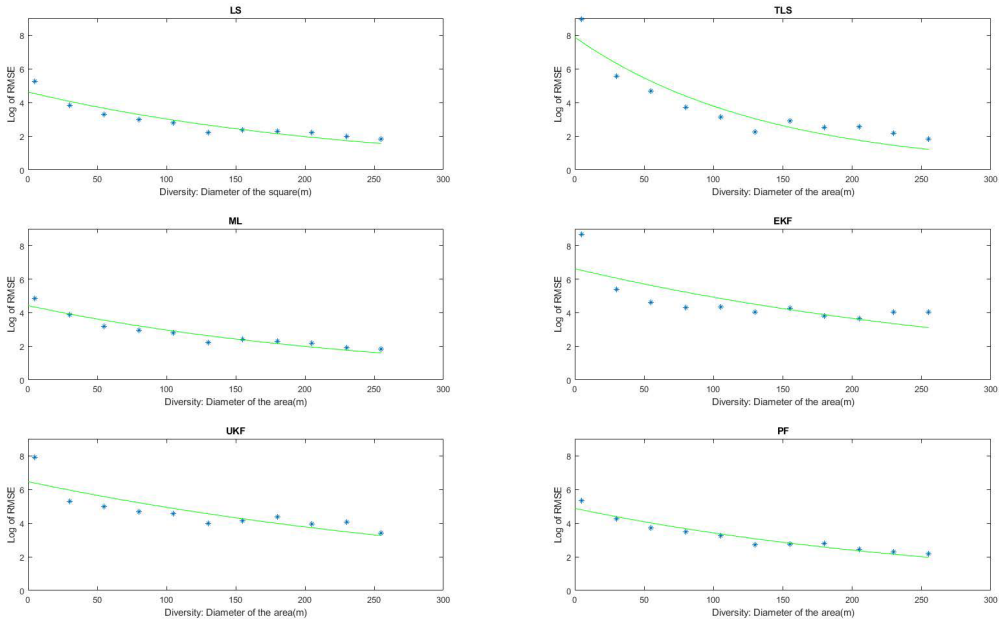

(a) Area diameter between 5m to 275m.

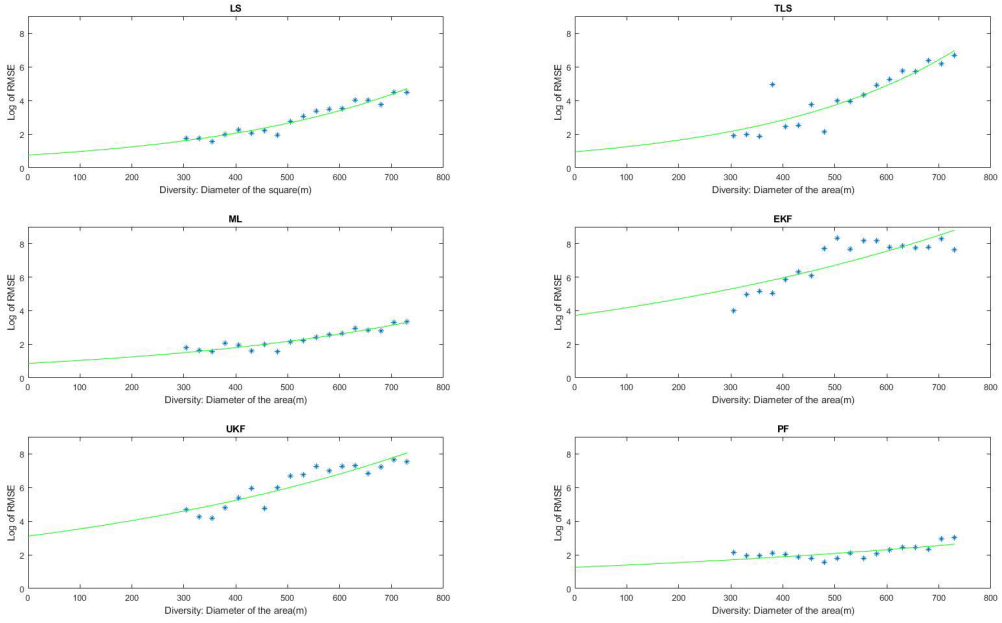

(b) Area diameter between 300m to 725m.

FIG. 6. (Color online) Plot of log of RMSE versus cluster diversity. (a) Area diameter between 5 and 275 m. (b) Area diameter between 300 and 725 m.

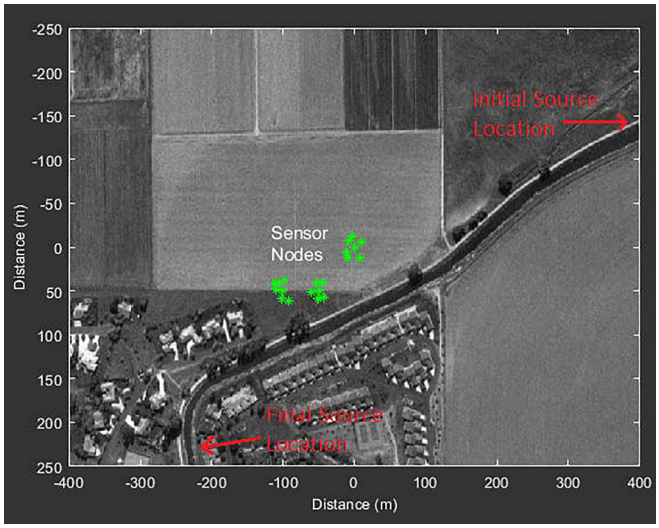

FIG. 7. (Color online) Aerial map of the simulated road.

for higher SNR, the sensor location errors have a more dominating effect.

Another important factor that also plays an important role in the source location estimation performance is the arrangement of the clusters with respect to each other. This would impact the ability to resolve DoAs or provide unique DoA for each cluster, and hence the localization accuracy. To investigate this effect, a simulation is done by changing the size of the area in which the clusters are deployed. More specifically, the clusters are located randomly in a circular area with varying diameter and the RMSE is calculated and averaged for 40 different random trials. Figure 6 shows the plot of the log of averaged RMSE for diameters ranging from 5 to 725 m. An exponential is fitted (green plot) to the data for providing better intuition. Again, several intriguing observations can be made here. Figure 6(a) illustrates that for diameters less than 275 m, RMSE decreases as the diameter (or equivalently cluster diversity) increases. That is, the larger the cluster distances, the better the performance of each estimator will be in the RMSE sense. On the other hand, Fig. 6(b) shows that the RMSE increases with the increase of the area diameter (roughly over 300 m). The degradation in performance is mainly due to propagation or coherence loss, particularly at far source ranges. However, this degradation is less prominent for the PF method.

Next, all the algorithms were evaluated for a simulated road case with bends and curves, which is a more realistic scenario than the previous case where the vehicle path was just along a straight line. Figure 7 shows the aerial map of the road that was used to generate the simulated cases for this experiment. The vehicle starts moving from the top-right corner of Fig. 7 at [400 150]. Three randomly distributed acoustic clusters with reference nodes at positions $\mathbf{r}_1 = [0, 0]$, $\mathbf{r}_2 = [-50, 50]$, and $\mathbf{r}_3 = [-100, 50]$ meters were used in this simulation. Acoustic TL was also taken into effect and the SNR = 5 dB at the CPA of the source to each sensor. All other conditions are identical to the previous experiment.

Figures 8(a)–8(f) show the plots of the true (p_x, p_y) and estimated $(\hat{p}_x, \hat{p}_y)$ positions of the moving vehicle generated using all six methods. The bars show the error standard deviations from the true source location for different estimators computed for 15 trials, where in each trial, the position of sensors within a cluster with fixed centroid were randomly changed as in the previous experiments. It can be seen from Figs. 8(d)–8(f) that the EKF, UKF, and PF methods exhibit much higher error standard deviations whenever the vehicle undergoes a change in direction and/or velocity. This is mainly due to a mismatch between the true vehicle dynamics and the assumed constant velocity motion model used in Eq. (11). Since the LS, TLS, or ML-based estimation procedures make no such assumption, their location estimates follow the true location estimates more closely than those of the UKF,

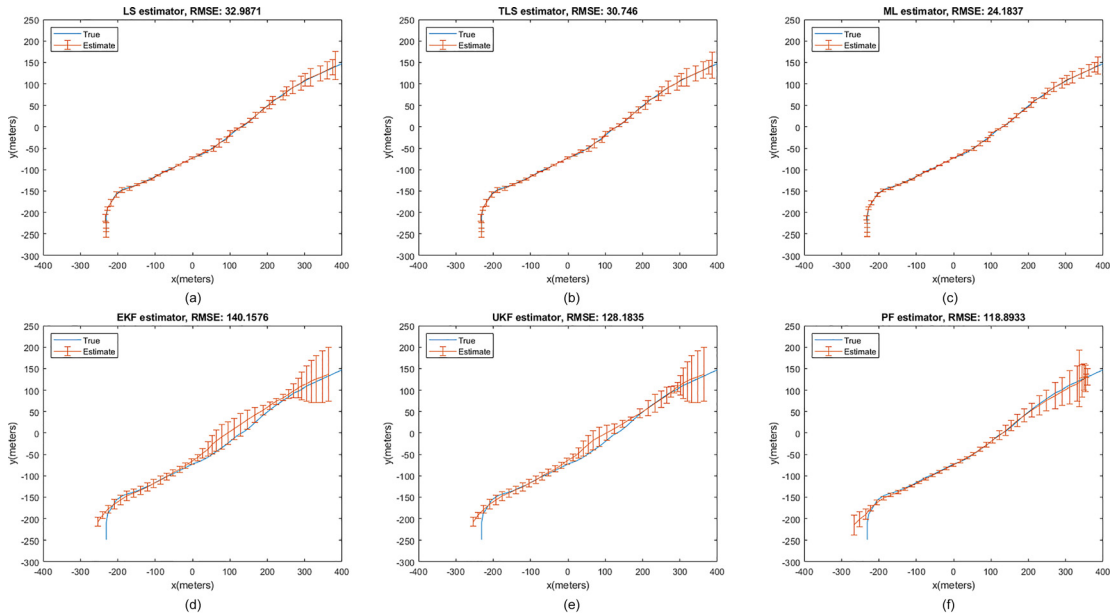

FIG. 8. (Color online) Position estimates of different localization methods for the simulated road, SNR = 5 dB. (a) LS, (b) TLS, (c) ML, (d) EKF, (e) UKF, and (f) PF.

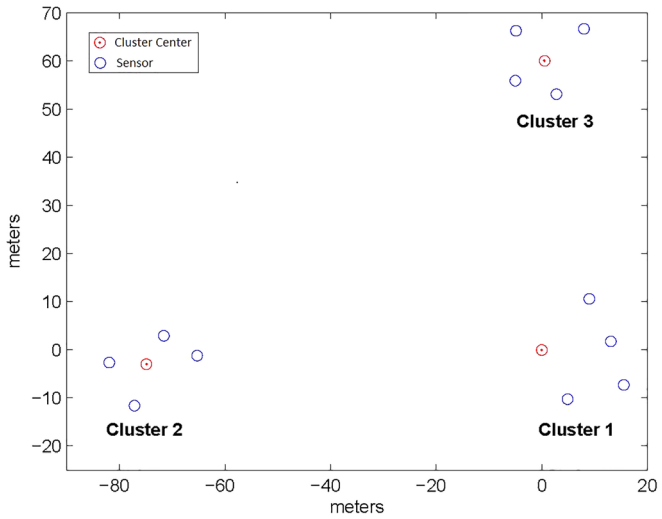

FIG. 9. (Color online) Clusters of randomly distributed acoustic sensor nodes.

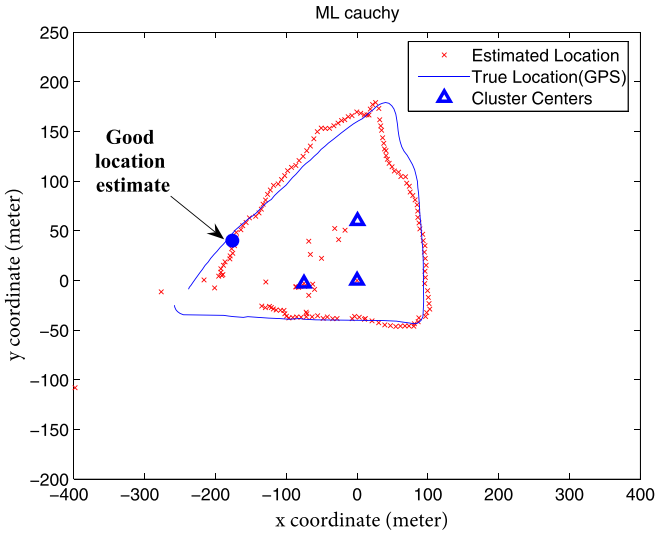

FIG. 11. (Color online) Estimated truck location against its true location for Run 1.

EKF, and PF estimators. Figure 8 also gives the corresponding average RMSE values of these source localization algorithms. As can be seen, the RMSE values are much higher for the EKF, UKF, and PF compared to those of the LS, TLS, or ML-based algorithms with the latter robust method providing the smallest RMSE value. These results are in contrast to those of the previous experiments for the fixed dynamical model cases. This implies that the EKF, UKF, and PF methods perform well when the vehicle dynamics are known or can be estimated accurately every time prior to localization. Overall, among these algorithms, the robust ML-based method provided the best results for this simulated data. Thus, this method is used in the next section to test its usefulness on real acoustic signature data sets.

B. Results on real data sets

In this setup, 15 wireless sensor nodes were randomly deployed in three clusters each of five nodes within an area of size 100×100 m. There were two adjacent roads, one to the south and one to the west of the deployment area with nominal traffic, which produced competing interference at times during the data collection process. The cluster centers are adequately spaced in order to guarantee DoA diversity given the maximum distance of the vehicle from the clusters. Figure 9 shows the deployment patterns of the sensor clusters. The cluster centers are marked as "⊙." The spatial coordinates of the center nodes in the three clusters are [0 0], [−74.92 −2.96], and [0.55 59.98] meters. During the data collection, the wind was minimal and at times was 5–7 mph. The vehicle used in this experiment was a light wheeled truck. The synchronized acoustic signature (engine and tire noise) data recorded and transmitted by the sensor nodes were received by a laptop that was used as the base station. A DoA is computed for every cluster at every one second snapshot using the wideband geometric averaging Capon algorithm in Sec. II A. The computed DoAs were then used to estimate the truck's 2 D location coordinates using the robust ML-based target localization algorithm in Sec. II C 4.

The results for two runs with different moving paths are presented here. Figures 10(a)–10(c) show the plots of the DoAs generated for clusters 1, 2, and 3, respectively, for Run 1. Continuous and smooth DoA estimates observed in all three clusters indicate that the sparsely distributed nodes are able to closely track the truck. Figure 11 shows the plot of the estimated truck location and the actual (measured) truck location. The actual truck location was provided by a simple and inexpensive hand-held GPS unit that is clearly error prone. There are many possible factors that contribute to producing inaccurate location estimates, namely, lower road elevations at certain points (north bend) during the vehicle path, competing interference due to adjacent road

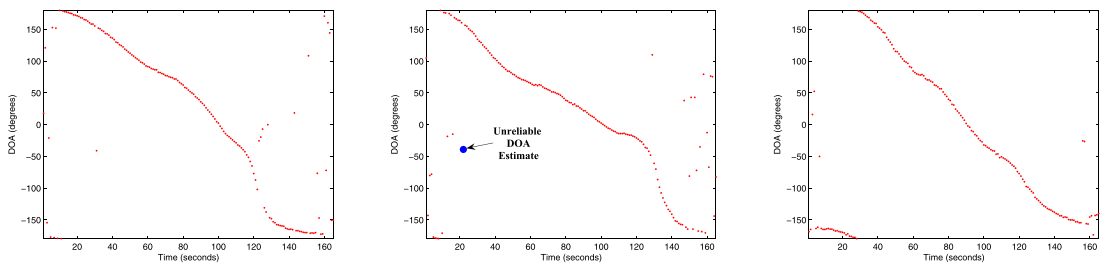

(a) DoA estimate of Cluster 1 (b) DoA estimate of Cluster 2 (c) DoA estimate of Cluster 3

FIG. 10. (Color online) DoA estimates from three clusters of five nodes for Run 1. (a) DoA estimate of Cluster 1, (b) DoA estimate of Cluster 2, and (c) DoA estimate of Cluster 3.

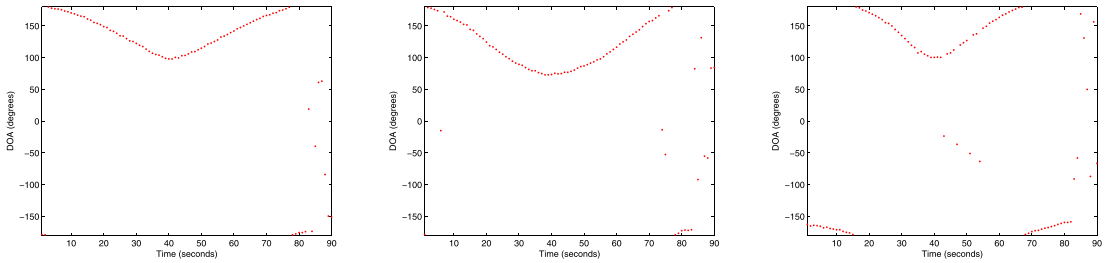

(a) DoA estimate of Cluster 1 (b) DoA estimate of Cluster 2 (c) DoA estimate of Cluster 3

FIG. 12. (Color online) DoA estimates from three clusters of five nodes for Run 2. (a) DoA estimate of Cluster 1, (b) DoA estimate of Cluster 2, and (c) DoA estimate of Cluster 3.

noise as well as wind, TL at far ranges, and finally compression noise for transmitting compressed data to the base station. However, it can be observed from this figure that the estimated locations closely follow the actual locations at most snapshots. In Fig. 10(b), we highlighted (blue) one particular snapshot at which the second cluster provided an unreliable DoA estimate. However, the accuracy of the location estimate was unaffected by the presence of this erroneous measurement as shown in Fig. 11. This is due to the robust source localization algorithm described in Sec. II C 4.

In the second run, the truck moved across the road and returned along the same path. This particular run was chosen to determine the resolution in localizing the moving truck on the same path during both the forward and return passes. The estimated DoAs for the three clusters are shown in Figs. 12(a)–12(c). The plot of the estimated truck location and the actual location are shown in Fig. 13. In this run, for most snapshots, there is little error between the estimated and actual truck locations. The same sources of error existed for this run. This particular experiment clearly indicates the good resolution of the distributed sensor networks in localizing moving sources.

IV. CONCLUSIONS

In this paper, we introduced and compared several methods for bearing-only target localization using multiple sparse randomly distributed acoustic sensor nodes. Simulation results indicated that the LS-based localization methods that use single snapshots are sensitive to erroneous DoA estimates and outliers. The nonlinear Kalman estimators and particle filtering that use the entire past and present sequence of observations, on the other hand, provide good localization accuracy as long as the assumed source dynamical model matches closely with its actual one. However, these conditions are not typically met in realistic moving source scenarios. Thus, to use EKF, UKF, or PF estimators, parameter estimation methods must be used to estimate the model parameters while performing state estimation.

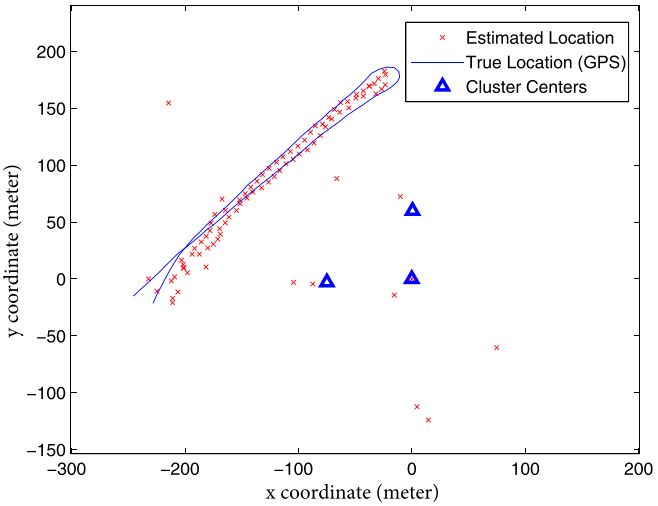

FIG. 13. (Color online) Estimated truck location against its true location for Run 2.

Additionally, the simulation results indicated that among the methods considered here, the PF is more robust to the decline in SNR. However, for SNR values higher than 8 dB, the performance of all methods is almost unaffected as the sensor location uncertainties have more dominant effects. We also showed that increasing the cluster placement diversity generally tends to improve the localization accuracy. Nevertheless, increasing the cluster separation beyond certain points will have detrimental effects due to propagation and coherence loss.

To make the ML-based localization robust against the erroneous DoAs and outliers, we proposed to model the measurement error as a rv with Cauchy distribution. This heavy tail distribution allows for a better ability to account for the effects of erroneous measurements or outliers. An additional provision was suggested to identify and remove inconsistent DoAs prior to final source localization. The results on real data sets showed the promise of the proposed algorithm using only three clusters of five low-cost low-power wireless sensor nodes. The experimental results conducted in this work indicated that it is possible to obtain accurate estimates of the vehicle position when the vehicle is less than approximately 200 m from the clusters. This is due to several possible reasons. First, the vehicle used in these experiments was a small truck that was not audible at far ranges compared to the background traffic noise coming from adjacent roads and low to mild wind at times. Second, at far distances, it is possible that the clusters observe nearly identical DoAs, hence violating the diversity needed for accurate localization. Finally, sound TL due to ground conditions and wind effects can impact the coherence in the recorded data.

ACKNOWLEDGMENTS

This work was supported by U.S. Army SBIR Phase II Contract Nos. DAAE30-03-C-1055 and W15QKN-06-C-0089.

[1]T. Pham and B. M. Sadler, "Wideband array processing algorithms for acoustic tracking of ground vehicles," Technical Report, ARL Technical Report, Army Research Laboratory, Adelphi, MD (1997).
[2]N. Srour, "Unattended ground sensors—A prospective for operational needs and requirements," Technical Report, ARL Report Prepared for NATO, Army Research Laboratory, Adelphi, MD (1999).
[3]T. Pham and M. Fong, "Real-time implementation of music for wideband acoustic detection and tracking," in *Proceedings of SPIE, Automatic Target Recognition VII* (1997).
[4]M. Hawkes and A. Nehorai, "Wideband source localization using a distributed acoustic vector-sensor array," IEEE Trans. Signal Process. **51**, 1479–1491 (2003).
[5]R. J. Kozick and B. M. Sadler, "Source localization with distributed sensor arrays and partial spatial coherence," IEEE Trans. Signal Process. **52**, 601–616 (2004).
[6]X. Sheng and Y.-H. Hu, "Maximum likelihood multiple-source localization using acoustic energy measurements with wireless sensor networks," IEEE Trans. Signal Process. **53**, 44–53 (2005).
[7]T. Ajdler, I. Kozintsev, R. Lienhart, and M. Vetterli, "Acoustic source localization in distributed sensor newtorks," in *Proceedings of the Thirty-Eighth Asilomar Conference on Signals, Systems and Computers*, Pacific Grove, CA (November 7–10, 2004), pp. 1328–1332.
[8]M. Cobos, F. Antonacci, A. Alexandridis, A. Mouchtaris, and B. Lee, "A survey of sound source localization methods in wireless acoustic sensor networks," Wireless Commun. Mobile Comput. **2017**, 3956282.
[9]J. Luo, X. Zhang, Z. Wang, and X. Lai, "On the accuracy of passive source localization using acoustic sensor array networks," IEEE Sens. J. **17**, 1795–1809 (2017).
[10]M. R. Azimi-Sadjadi, N. Roseveare, and A. Pezeshki, "Wideband DOA estimation algorithms for multiple moving sources using unattended acoustic sensors," IEEE Trans. Aerosp. Electron. Syst. **44**, 1585–1598 (2008).
[11]K. Dogancay, "Bearings-only target localization using total least squares," Signal Process. **85**, 1695–1710 (2005).
[12]S. J. Julier and J. K. Uhlmann, "Unscented filtering and nonlinear estimation," Proc. IEEE **92**, 401–422 (2004).
[13]B. Ristic and M. S. Arulampalam, "Tracking a manoeuvring target using angle-only measurements: Algorithms and performance," Signal Process. **83**, 1223–1238 (2003).
[14]Q. Le, L. M. Kaplan, and J. H. McClellan, "Kalman filtering using bearings-only measurements from a network of acoustic arrays," in *Proceedings of the 10th Digital Signal Processing Workshop*, Pine Mountain, GA (October 16, 2002).
[15]D. B. Ward, E. A. Lehmann, and R. C. Williamson, "Particle filtering algorithms for acoustic source localization," IEEE Trans. Speech Audio Process. **11**, 826–836 (2003).
[16]S. Thrun, W. Burgard, and D. Fox, *Probabilistic Robotics* (The MIT Press, Cambridge, MA, 2006).
[17]E. Chong and S. H. Zak, *An Introduction to Optimization* (Wiley Series in Discrete Mathematics and Optimization, New York, 2013).
[18]R. B. Schnabel and E. Eskow, "A new modified Cholesky factorization," SIAM J. Sci. Comput. **11**, 1136–1158 (1990).
[19]G. Wichern, M. R. Azimi-Sadjadi, and M. Mungiole, "Environmentally adaptive acoustic transmission loss prediction in turbulent and nonturbulent atmospheres," Neural Netw. **20**, 484–497 (2007).
[20]L. M. Kaplan and Q. Le, "On exploiting propagation delays for passive target localization using bearings-only measurements," J. Franklin Inst. **342**, 193–211 (2005).